ACS APPLIED MATERIALS & INTERFACES

Research Article

www.acsami.org

Lindqvist Polyoxoniobate Ion-Assisted Electrodeposition of Cobalt and Nickel Water Oxidation Catalysts

YuPing Liu, Si-Xuan Guo, Liang Ding, C. André Ohlin, Alan M. Bond,* and Jie Zhang*

School of Chemistry and Australian Research Council Centre of Excellence for Electromaterials Science, Monash University, Clayton, Victoria 3800, Australia

ABSTRACT: A method has been developed for the efficient electrodeposition of cobalt and nickel nanostructures with the assistance of the Lindqvist ion $[Nb_6O_{19}]^{8-}$. Scanning electron microscopy (SEM), energy-dispersive X-ray spectroscopy (EDX), Raman spectroscopy, inductively coupled plasma mass spectrometry (ICP-MS), inductively coupled plasma optical emission spectrometry, and a range of electrochemical techniques have been used to characterize the morphology, composition, catalytic water oxidation activity and stability of the films in alkaline solution. SEM images show that films consisting of nanoparticles with diameters of ca. 30 to 40 nm are formed after 40−50 potential cycles of deposition. Nb and Co/Ni are detected in the films by EDX. ICP-MS results show an elemental ratio of 1:1 for Co:Nb and 1:3 for Ni:Nb, respectively. Raman spectra reveal the presence of both $[Nb_6O_{19}]^{8-}$ and $Co(OH)_2/Ni(OH)_2$. The films exhibit excellent stability and efficiency for electrocatalytic water oxidation in alkaline solution. Turnover frequencies of 12.9 and 13.2 s^{-1} were determined by rotating ring disk electrode voltammetry at an overpotential of 480 mV for Co and Ni films, respectively. Fourier transformed large amplitude alternating current (FTAC) voltammetry reveals an additional underlying oxidation process for Co under catalytic turnover conditions, which indicates that a Co^{IV} species is involved in the efficient catalytic water oxidation reactions. FTAC voltammetric data also suggest that the Ni films undergoes a clear phase transformation upon aging in aqueous 1 M NaOH and the electrogenerated higher oxidation state Ni from β-NiOOH is the more active form of the catalyst.

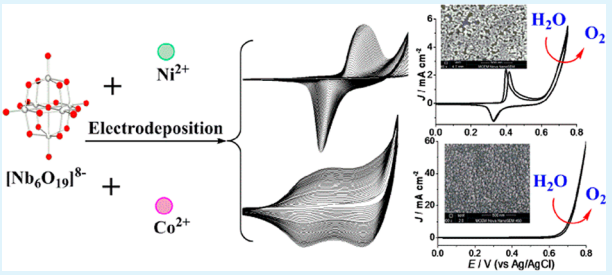

KEYWORDS: *water oxidation, electrodeposition, cobalt, nickel, polyoxometalate, niobate*

1. INTRODUCTION

Electrochemically driven water splitting is a major focus of sustainable energy research. The hydrogen evolution aspect of water splitting is now fairly well understood and can be achieved with low overpotential.[1] Recently, most attention therefore has been paid to water oxidation because of its slow kinetics which lead to large overpotentials.[2] Although both molecular[3,4] and nanostructured noble metal oxides catalysts, such as RuO_2[5] and IrO_2,[6] have been widely explored, Co- and Ni-based catalysts are still of great interest because they are efficient, earth abundant, and low cost. In particular, nickel metal and alloys, cobalt metal,[7−9] their oxides,[10,11] and hydroxides[12] have been investigated as electrocatalysts for water oxidation, especially under alkaline conditions where the metal (hydr)oxides are insoluble. In basic media, the half-cell reaction for oxygen evolution at the anode electrode is described by eq 1[13]

$$4OH^- \rightarrow O_2 + 2H_2O + 4e^- \quad (1)$$

Ni and Co (hydr)oxide films have been prepared by sol−gel, thermal decomposition, solution casting, electrodeposition and other methods.[13−16] The overall composition, Co or Ni content, thickness, morphology and the way the films are attached to the electrodes are a function of the preparation methods, and determine the activity and stability of the catalysts. Generally, it is easier to control the film thickness and particle size by electrodeposition.[17] CoO_x films formed by oxidative electrodeposition from Co^{II} solution in the presence of inorganic phosphate, borate, and other buffered electrolytes have been studied by Nocera and co-workers.[18−21] Their work, together with the study by Gerken et al.,[22] have provided insights into the catalytic water oxidation mechanism using a CoO_x film, and led to the proposal that the O−O bond formation step involves the reaction of water with oxo Co^{IV}. For Ni, the hydroxide (β-$Ni^{III}OOH$), which is formed in concentrated alkaline solutions, was proposed as the active catalyst,[8,23] but electrochemical and spectroscopic evidence has also implied the involvement of Ni^{IV}.[24−26]

Polyoxometalates (POMs) are a family of molecular oxides.[27,28] POMs have been used to synthesize and stabilize nanoparticles since they are highly negatively charged and their reduced forms are strong reducing agents.[29−31] Polyoxoniobates and -tantalates are unique among POMs owing to their high stability under alkaline conditions.[32,33] Of the niobates, the Lindqvist ion, $[Nb_6O_{19}]^{8-}$ (now referred to as NbPOM; see Figure 1), has the highest charge density, is stable above pH

Received: May 15, 2015
Accepted: July 9, 2015
Published: July 9, 2015

DOI: 10.1021/acsami.5b04219
ACS Appl. Mater. Interfaces 2015, 7, 16632−16644

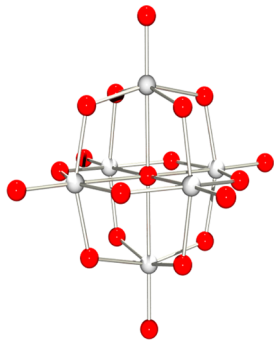

Figure 1. Ball-and-stick representation of the structure of the Lindqvist ion $[Nb_6O_{19}]^{8-}$. Nb and O atoms are presented gray and red, respectively.

9.5,[34] and has the additional advantage of being straightforward to synthesize on the gram scale.[35] In aqueous solution, $[Nb_6O_{19}]^{8-}$ is polyprotic and self-buffering over the pH range of 10 to 12.5 when present at a concentration of 4.5 mM.[34] Co and Ni cations have been shown to coordinate with NbPOM to generate new polyoxometalates under elevated temperature conditions.[36,37] On the basis that NbPOM will at least form ion pairs with cobalt and nickel cations,[36−39] it is proposed that new catalytic features may be introduced into the electrodeposited films.

In this paper, a Lindqvist POM, $K_7H[Nb_6O_{19}]$, was used to assist the electrodeposition of Co and Ni (hydr)oxide films. The electrodeposited Co and Ni (hydr)oxide films were characterized using a range of spectroscopic, microscopic and electrochemical techniques. The application of electrodes modified with these films for water oxidation was explored in alkaline media.

2. EXPERIMENTAL SECTION

2.1. Material. Cobalt nitrate ($Co(NO_3)_2{\cdot}6H_2O$, ≥ 99.0%), niobium pentoxide (Nb_2O_5, 99.9%), and potassium hydroxide (KOH, ≥ 85%) from Sigma-Aldrich, sodium hydroxide (NaOH, 99.0%, Merck), and nickel nitrate ($Ni(NO_3)_2{\cdot}6H_2O$, ≥ 98.5%, M&B laboratory chemicals) were used as supplied. Deionized water from a Milli-Q-MilliRho purification system (resistivity 18 MΩ cm) was used to prepare all aqueous electrolyte solutions. Nitric acid (65%, ISO grade) and hydrofluoric acid (48%, ultrapure) are from Merck and distilled before use for inductively coupled plasma mass spectrometric (ICP-MS) and inductively coupled plasma optical emission spectrometric (ICP-OES) analysis.

2.2. Preparation of Potassium Hexaniobate, $K_7HNb_6O_{19}{\cdot}18H_2O$. The general method of Britton and Robinson[35] was modified to give the procedure outlined below. Anhydrous Nb_2O_5 (2.0 g) was added in small portions to molten KOH (85%, 7.0 g) contained in a Ni crucible and heated with a Bünsen burner. Once addition was complete, the molten mixture was heated for a further 15 min, before being allowed to cool to give a solid. Boiling water (20 mL) was added to dissolve the solidified mass, before gravity filtering the hot solution. The filtrate was stored in a beaker sealed with parafilm and left overnight in a freezer. The transparent and colorless $K_7HNb_6O_{19}{\cdot}18H_2O$ crystals were collected by filtration (1.563 g, 1.1 mmol). The filtrate volume was reduced by half on a rotary evaporator, and placed in a freezer for 8 h, yielding an additional 0.941 g (0.7 mmol) of crystalline product. The overall yield was 72% with respect to niobium, assuming 18 water molecules of crystallization are present per molecule of hexaniobate ion ($K_7HNb_6O_{19}{\cdot}18H_2O$).

2.3. Electrochemical Measurements. Conventional dc cyclic voltammetric and rotating ring disk electrode (RRDE) experiments were carried out with a CHI 760D electrochemical workstation (CH Instruments, Austin, Texas, USA). A Rotating Disk Electrode Rotator (RRDE-3A, ALS Co., Japan) connected to a CHI 760D electrochemical workstation was used for RRDE experiments. To obtain Tafel plots with minimal effect from uncompensated resistance (R_u), iR_u compensation (i = current) was applied during cyclic voltammetric experiments over the potential range of 0.0 to +0.75 V. R_u was first measured at a potential where no faradaic current was present via use of RC time constant method available on the CHI 760D potentiostat. iR_u compensation with this resistance value was then applied automatically by the instrument during cyclic voltammetric experiment over the desired potential range. Fourier transformed large amplitude ac (FTAC) voltammetric measurements were undertaken with home-built apparatus,[40] using an applied sine wave perturbation of known frequency (f) and amplitude (ΔE) superimposed onto the dc ramp. The total current measured from application of the waveform was then subjected to Fourier transformation to obtain a power spectrum. After selection of the frequency band of interest, inverse Fourier transformation was used to generate the required aperiodic dc or ac harmonic components.[40,41]

All voltammograms were acquired at 22 ± 2 °C. A standard three-electrode electrochemical cell arrangement was employed using a glassy carbon (GC) working electrode (1.0 or 3.0 mm diameter, CH Instruments, Austin, Texas, USA), a Pt wire counter electrode and a Ag/AgCl (3 M NaCl) reference electrode (0.210 V vs SHE).[42] A RRDE working electrode with a GC disk (4.0 mm diameter) and a Pt ring (5.0 mm ID: 7.0 mm OD, ALS Co., Japan) was used for the RRDE studies along with the same reference and counter electrodes employed in dc and FTAC voltammetry. Prior to each series of experiments, the working electrode was polished with an aqueous 0.3 μm alumina slurry on a polishing cloth (Buehler), rinsed with water, and then sonicated to remove alumina, before a final rinse with water. Before each experiment, the solution was purged with nitrogen for at least 3 min to remove O_2, and then a positive pressure of nitrogen was maintained above the solution for the duration of the measurement. A platinum electrode with a removable tip (2 mm diameter, AiDaHengSheng, China) was used to electrodeposit films for Raman measurements, while a GC electrode with a removable tip (3 mm diameter, AiDaHengSheng, China) was used to electrodeposit films for scanning electron microscopy (SEM) imaging and energy-dispersive X-ray (EDX) analysis.

To evaluate the water oxidation catalytic activity of the films, we used a GC electrode for electrodeposition of the films by cycling the potential in a selected range for desired number of cycles. The modified GC electrode was then removed from the solution, and washed with deionized water several times to remove any free Co^{2+}, Ni^{2+}, or NbPOM from the electrode surface. Finally, the modified electrode was placed in a 1 M NaOH solution for electrocatalytic oxidation of water.

2.4. Other Instrumentations. SEM images and EDX spectra were collected with a FEI Nova NanoSEM 450 FEG SEM electron microscope. Dynamic light scattering measurements were performed with a Brookhaven Zeta Plus instrument. Raman spectra were recorded on a Renishaw inVia Raman microscope with a 1.0 mW laser power setting at 514 nm. ICP-MS with a GBC OptiMass 9500 ICP TOF-MS and a Thermo ICAP Duo 7400 ICP-OES were used to analyze the compositions of the electrodeposited films. To prepare samples for ICP analysis, the Co−Nb and Ni−Nb films were electrodeposited on 3 mm diameter GC electrodes, rinsed with deionized water and dried. The films were then dissolved in a 0.7 mL concentrated HNO_3 and HF mixture (5:2 volume ratio). Excess HF was evaporated by heating at 50 °C and the solution was diluted with water to 10 mL prior to the ICP-MS or ICP-OES analysis. Calibration curves were constructed using commercially available Co, Ni, Nb, and Fe standard solutions. Yttrium was used as an internal standard.

3. RESULTS AND DISCUSSION

3.1. Electrodeposition of Co- and Ni-Containing Films from Aqueous Electrolyte Media Containing 5 mM $K_7HNb_6O_{19}$. To prepare solutions for electrodeposition of the films, the required volume of a $M(NO_3)_2$ (M = Co or Ni) stock

DOI: 10.1021/acsami.5b04219
ACS Appl. Mater. Interfaces 2015, 7, 16632−16644

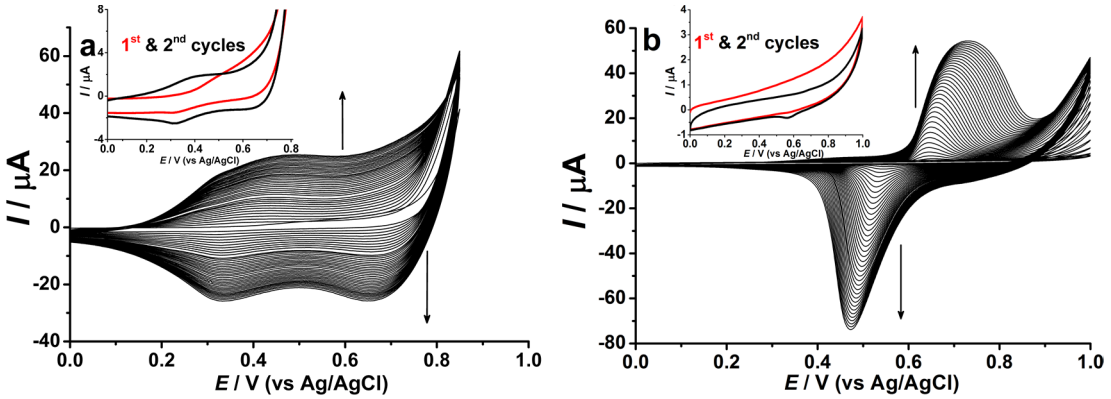

Figure 2. Cyclic voltammograms obtained at a GC electrode (3 mm diameter) with a scan rate of 0.1 V s^{-1} showing the increase of current that occur upon repetitive cycling of potential over the range of (a) 0.0−0.85 V with a 5 mM $Co(NO_3)_2$ and 5 mM NbPOM aqueous solution and (b) 0.0−1.0 V, with a 5 mM $Ni(NO_3)_2$ and 5 mM NbPOM aqueous solution. Insets show the initial two cycles of the voltammograms.

solution was added to a solution of $K_7HNb_6O_{19}$ to provide a final concentration of 5 mM for each component. After thorough mixing, the solutions have a light purple color (Co solution, now referred to as Co−Nb) or a light green color (Ni solution, now referred to as Ni−Nb) with a pH of ∼10. The solutions were checked with a red laser light beam to confirm the absence of scattering from precipitated oxides. Niobate plays an important role as a stabilizing agent, as evidenced by the fact that precipitates formed for both Co and Ni solutions at similar pH in the absence of niobate. Dynamic light scattering measurement over a 24 h period showed no evidence for nanoparticle formation and the solutions remained homogeneous. Thus, it is assumed that in solutions, Co and Ni ions are stabilized by $[Nb_6O_{19}]^{8-}$ through formation of ion-pairs as suggested in a previous study[43] rather than through the electrostatic stabilization of colloidal nanoparticles of $M(OH)_x$. Electrodeposition was carried out by cycling the potential from 0.0 to 0.85 V for Co and 0.0 to 1.0 V for Ni. As seen in Figure 2a, a broad process appears from about 0.3 to 0.5 V in the positive potential scan direction of the first cycle, with a sharper increase of current detected at about 0.75 V. On reversing the scan direction, two broad reduction processes are detected with peak potentials at 0.62 and 0.31 V. In the second cycle, a new process emerges at 0.41 V. Upon repetitive cycling of the potentials, oxidation and reduction currents continuously increase. A small oxidation process also emerges at 0.31 V after several cycles of potential. For Ni deposition (Figure 2b), no well-defined process is observed in the initial cycle. A small oxidation process at 0.65 V together with a small reduction process at 0.55 V are observed in the second voltammetric cycle. The oxidation process at 0.65 V shifts positively upon cycling of the potential, whereas the reduction process at 0.55 V shifts negatively. The continuous increase in current upon potential cycling suggests the successful deposition of a solid film. Different ratios of Co or Ni to Nb (the initial concentrations of Co^{2+} or Ni^{2+} were kept constant) were also tested for electrodeposition of hydr(oxide), but a 1:1 ratio provided the best deposition efficiency as defined by the largest current per cycle of potential.

3.2. Characterization of the Deposited Films. Details of the morphology and composition of both the Co- and Ni-containing films were obtained ex situ from SEM images, EDX and elemental analysis. The SEM image in Figure 3a reveals that the film formed on a GC electrode after 40 cycles of potential in the Co−Nb solution consists of ca. 30 nm diameter

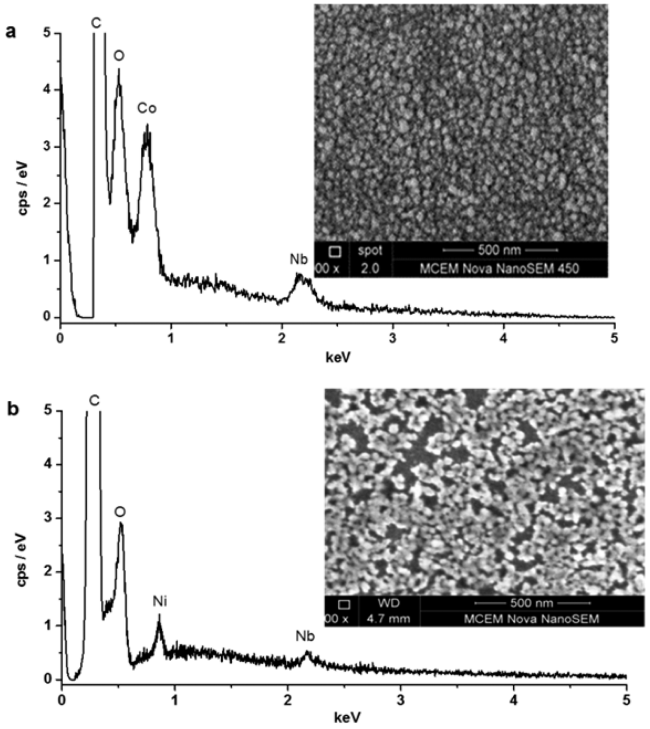

Figure 3. SEM images and EDX spectra of the (a) Co and (b) Ni films deposited on a GC electrode by scanning the potential over the range of (a) 0.0−0.85 V for 40 cycles in a Co−Nb solution, and (b) 0.0−1.0 V for 50 cycles in a Ni−Nb solution.

nanoparticles. EDX spectrum of the film derived from the Co−Nb solution show the presence of Co, Nb, C and O (Figure 3a). Carbon and at least some of the oxygen are from the GC electrode. ICP-MS analysis shows that the elemental ratio of Nb to Co in this film is close to 1:1. A SEM image of the Ni−Nb film (Figure 3b) obtained after 50 cycles of potential with a GC electrode shows the presence of ca. 40 nm diameter nanoparticles. EDX spectrum shown in Figure 3b also confirms the presence of Nb and Ni, along with other elements associated with the GC electrode substrate. The ICP-MS result obtained for the Ni−Nb film gives a Ni:Nb ratio of 1:3.

To probe the chemical nature of the electrodeposited Ni−Nb and Co−Nb films, XRD and Raman measurements were undertaken. However, no well-defined XRD spectrum was obtained, plausibly because of the amorphous nature of the

DOI: 10.1021/acsami.5b04219
ACS Appl. Mater. Interfaces 2015, 7, 16632−16644

deposited films. The Raman spectrum obtained for the Co−Nb film deposited on a Pt electrode (Figure 4a) shows a dominant

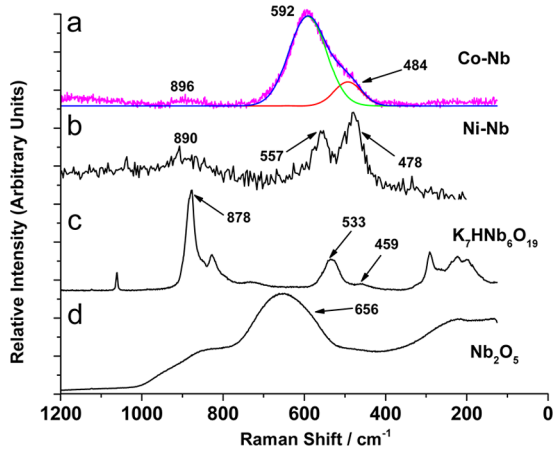

Figure 4. Raman spectra obtained on the (a) Co−Nb and (b) Ni−Nb films deposited at a Pt electrode by scanning the potential over the range of 0.0 to 0.85 V for 200 cycles in a Co−Nb solution and 0.0 to 1 V for 200 cycles in a Ni−Nb solution. Raman spectra of (c) $K_7HNb_6O_{19}\cdot 18H_2O$ and (d) Nb_2O_5 powders are also shown for comparison.

broad band at 592 cm^{-1} with a small shoulder at 484 cm^{-1} and a weak band at 896 cm^{-1}. The Raman spectrum obtained from the Ni−Nb film under the same conditions (Figure 4b) shows two dominant bands at 478 and 557 cm^{-1} with a weak broad band again being detected at about 890 cm^{-1}. The Raman spectra of $K_7HNb_6O_{19}\cdot 18H_2O$ and Nb_2O_5 powders are also included in this figure for comparison purposes. $K_7HNb_6O_{19}$ shows vibrational bands at 197, 220, 291, 459, 533, 827, 878 (dominant band), and 1061 cm^{-1}, whereas Nb_2O_5 shows a broad band at 656 cm^{-1}. Therefore, the small broad band at ~890 cm^{-1} may be attributed to the presence of $[Nb_6O_{19}]^{8-}$. Deconvolution of the Co−Nb Raman spectrum in the range of 400 to 800 cm^{-1} confirms that the observed response in this region is a result of two overlapping bands with peaks at 484 and 592 cm^{-1}, suggesting the presence of $Co(OH)_2$.[44,45] The bands with peaks at 478 and 557 cm^{-1} in the Ni−Nb films are assigned to γ-NiOOH residues from the oxidation of amorphous α-$Ni(OH)_2$ whose Raman peaks are not visible because of their relatively low intensity.[16,46] On the basis of the Raman evidence, it is likely that $[Nb_6O_{19}]^{8-}$ stabilizes $Co(OH)_2$ and $Ni(OH)_2$ nanoparticles via an electrostatic mechanism proposed for other polyoxometalate stabilized nanoparticles.[30,31]

3.3. Electrocatalytic Oxidation of Water in 1 M NaOH Aqueous Electrolyte. Dc cyclic voltammograms (Figure 5a) over the potential range of 0 to 0.8 V obtained with the Co−Nb film in 1 M NaOH exhibit a surface confined chemically reversible couple at 0.09 V (process **I**) in the first cycle of potential. The oxidation component of this couple shifts about 38 mV to more negative potential in the second cycle of potential. At more positive potentials, a broad oxidation process with a peak potential of around 0.47 V (process **II**) is found. On reversing the scan direction, a broad reduction one around 0.53 V is detected. FTAC voltammetry (Figure 5b) was used to further characterize the electrodeposited film using an amplitude of 160 mV and a frequency of 18.0 Hz. In the higher-order components of FTAC voltammetry, the con-

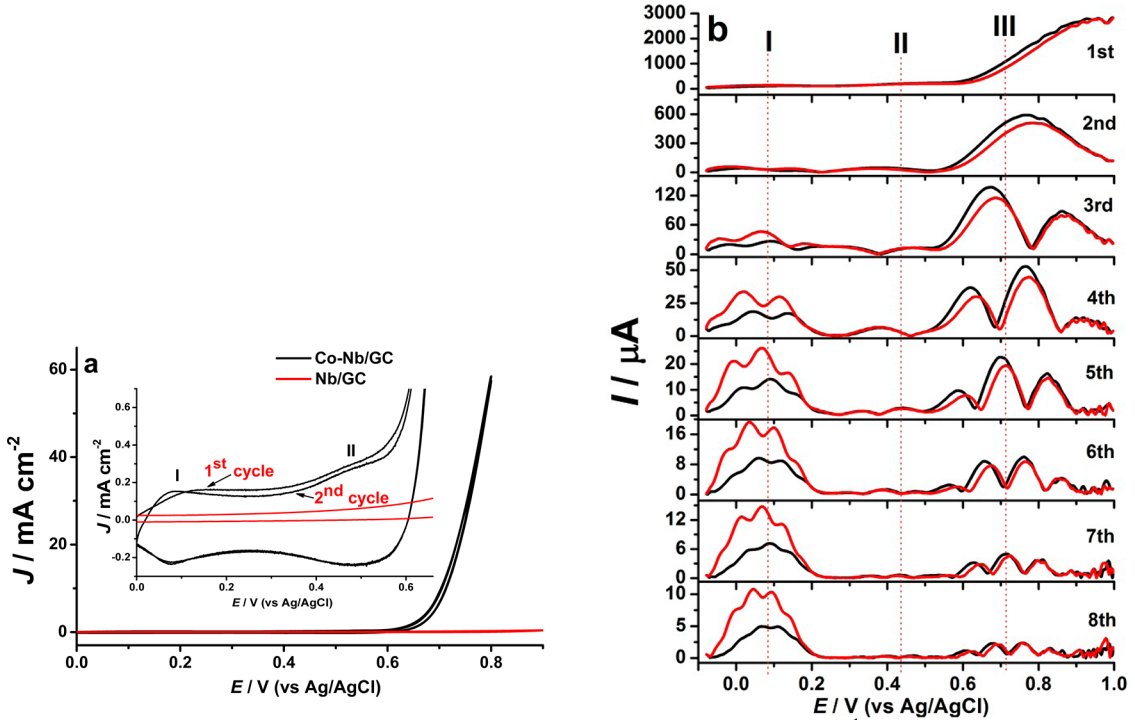

Figure 5. (a) Cyclic voltammograms obtained with a scan rate of 0.1 V s^{-1} in 1 M NaOH at a GC electrode (3 mm diameter) after deposition of a film (20 cycles of potential) from a Co−Nb solution (black, Co−Nb/GC) and a GC electrode modified with 5 μL 1 mM NbPOM (red, Nb/GC). Inset shows the cobalt based processes in the potential range of 0 to +0.6 V. (b) 1st to 8th harmonic FTAC voltammetry components (f = 18.0 Hz, ΔE = 160 mV, scan rate =0.081 V s^{-1}) obtained in 1 M NaOH at a 1 mm diameter GC electrode after 20 potential cycles of film deposition. (Black) forward scan (positive potential scan direction), and (red) reverse scan (negative potential scan direction).

DOI: 10.1021/acsami.5b04219
ACS Appl. Mater. Interfaces 2015, 7, 16632−16644

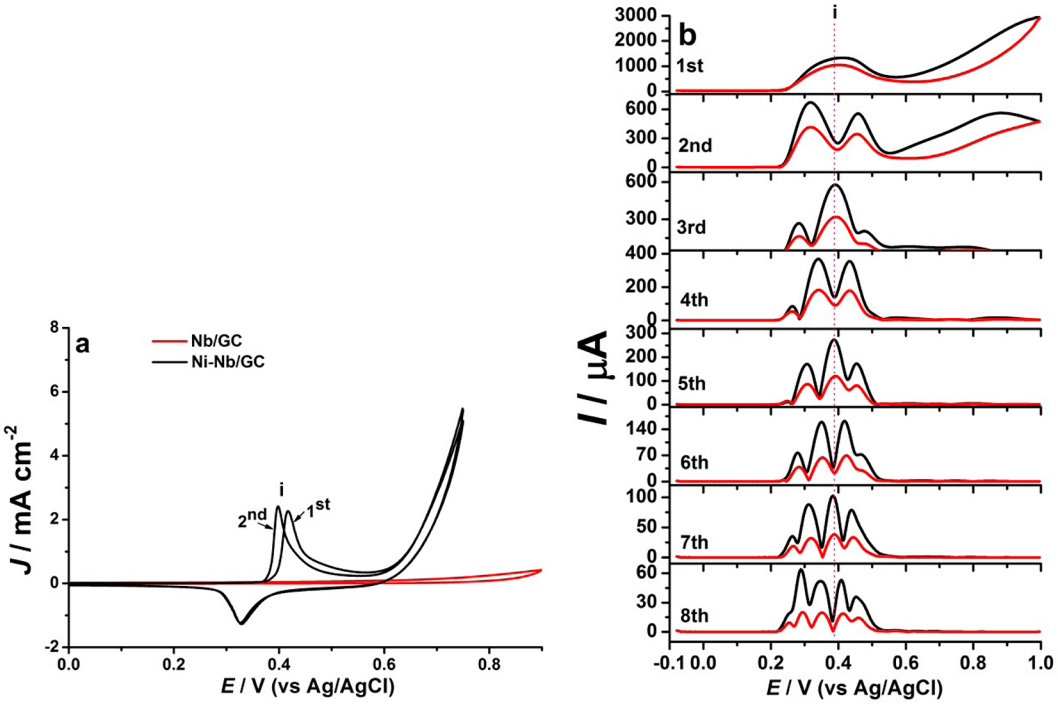

Figure 6. (a) Dc cyclic voltammograms obtained in 1 M NaOH with a scan rate of 0.1 V s^{-1} at a GC electrode (3 mm diameter) after deposition of a film (40 cycles of potential) from a solution containing 5 mM $Ni(NO_3)_2$ and 5 mM NbPOM (black, Ni−Nb/GC) and a GC electrode modified with 5 μL 1 mM NbPOM (red, Nb/GC). (b) 1st to 8th harmonic components (f = 9.0 Hz, ΔE = 160 mV, scan rate =0.081 V s^{-1}) obtained at a 3 mm diameter GC electrode after 40 potential cycles of film deposition. (Black) positive potential scan direction and (red) negative potential scan direction.

tributions from either the double layer charging or the catalytic water oxidation processes are negligible.[9,47] Therefore, the underlying electron transfer processes associated with the Co−Nb film are more clearly defined. In the fifth harmonic component, three processes are evident with maximum current values at 0.08 V (process **I**), 0.44 V (process **II**) and 0.71 V (process **III**) (Figure 5b). Process **III**, which is well-defined under FTAC voltammetric conditions, is undetectable under dc cyclic voltammetric conditions due to the presence of the catalytic water oxidation process. In FTAC voltammetry, the peak current magnitude depends on the electrode kinetics with faster processes giving larger currents. Process **II** has a much smaller peak current than processes **I** and **III**, which is attributed to its slower kinetics according to a previous study.[9] Processes **I** and **III** are fast but not fully reversible under FTAC voltammetric conditions as peak currents are not linearly dependent on the frequency in the range from 4.5 to 27.0 Hz. Rather, they are quasi-reversible as the peak current approaches a limiting value at the higher frequency.[48] In process **I**, the oxidation peak heights associated with ac harmonic components are smaller than the reduction ones despite the fact that the peak areas are comparable under dc cyclic voltammetric conditions (i.e., the process is chemically reversible). Peak currents associated with the ac harmonic components are highly sensitive to uncompensated resistance as well as electron transfer kinetics.[49] Therefore, the higher peak currents observed for the reduction component of process **I** may suggest that the oxidized form of Co−Nb film is less resistive or the kinetics of the overall reduction process is faster. However, speculation of the exact origin of this difference in peak heights is difficult because of the complexity of this solid-state process.

On the basis of the literature reports, the overall reactions associated with three processes detected under FTAC voltammetric conditions are assigned as follows,[7,15,50−52] without specifying the role of Nb.

$$3Co(OH)_2 + 2OH^- \rightleftharpoons Co_3O_4 + 4H_2O + 2e^- \text{ (process I, fast)} \quad (2)$$

$$Co_3O_4 + H_2O + OH^- \rightleftharpoons 3CoOOH + e^- \text{ (process II, slow)} \quad (3)$$

$$CoOOH + OH^- \rightleftharpoons CoO_2 + H_2O + e^- \text{ (process III, fast)} \quad (4)$$

Thus, process **I** is assigned to the oxidation of a Nb derivative of $Co(OH)_2$ to Co_3O_4, which is then converted to CoOOH at around 0.44 V (process **II**). The higher harmonic components of FTAC voltammetry are insensitive to the background and catalytic currents, so process **III** is well-defined at a potential even more positive than the dc voltammetric onset potential for water oxidation.[53] A current density of 6.1 mA cm^{-2} was achieved for water oxidation at an overpotential ($\eta = V_{appl} - iR_u - E^{0\prime}$, where the reversible potential $E^{0\prime}$ = 0.21 vs Ag/AgCl[9] at pH 14) of 480 mV under dc cyclic voltammetric conditions (Figure 5a). When the potential was scanned to the positive direction where process **III** is detected by FTAC voltammetry, gas bubbles were evident and accumulated on the electrode surface. By contrast, no appreciable water oxidation current was detected at a GC electrode modified with NbPOM (sparingly soluble in aqueous 1 M NaOH) (Figure 5a), which suggests that cobalt is responsible for the observed catalytic water oxidation activity of Co−Nb modified electrodes.

Cyclic voltammograms (Figure 6a) obtained with a Ni−Nb film formed from deposition for 40 cycles reveal a well-defined

DOI: 10.1021/acsami.5b04219
ACS Appl. Mater. Interfaces 2015, 7, 16632−16644

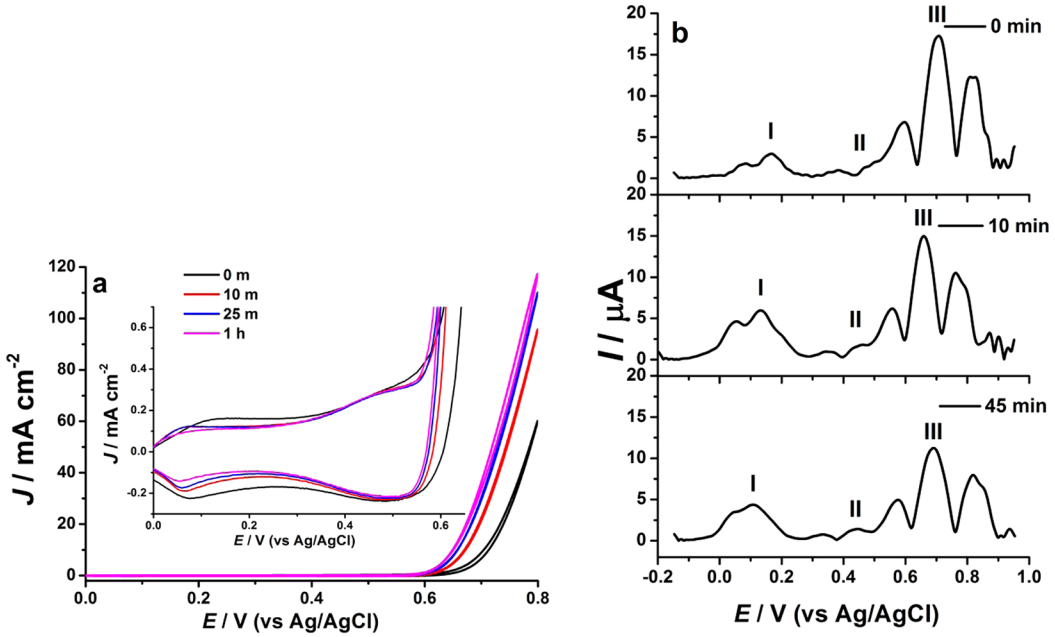

Figure 7. (a) Cyclic voltammograms obtained in 1 M NaOH with a scan rate of 0.1 V s^{-1} at a 3 mm diameter GC electrode modified with a Co−Nb film obtained with 20 cycles of potential for film deposition before (black) and after aging in 1 M NaOH solution for 10 min (red), 25 min (blue), and 1 h (magenta); Inset shows the cobalt based processes in the potential range of 0 to +0.6 V. (b) Fifth harmonic components derived from FTAC voltammograms obtained at the same electrode before and after aging in 1 M NaOH for 10 and 45 min. f = 9.0 Hz, ΔE = 160 mV, v = 0.080 V s^{-1}.

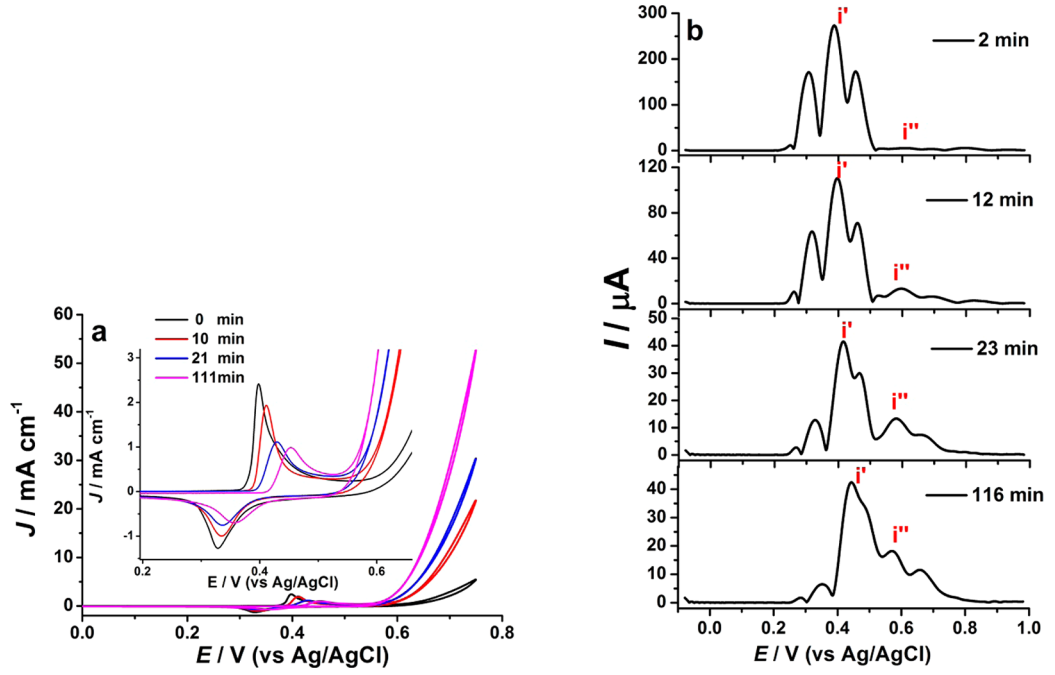

Figure 8. (a) Cyclic voltammogram obtained in 1 M NaOH with a scan rate of 0.1 V s^{-1} at a 3 mm diameter GC electrode modified with a Ni−Nb film obtained with 40 cycles of potential for film deposition before (black) and after aging for 10 min (red), 21 min (blue), and 116 min (magenta); Inset shows the nickel based processes in the potential range of 0.2 to +0.6 V. (b) fifth harmonic components derived from FTAC voltammograms obtained at the same electrode after aging in 1 M NaOH for 2, 12, 23, and 116 min. f = 9.02 Hz, ΔE = 160 mV, v = 0.080 V s^{-1}.

surface confined redox couple (process **i**) with an oxidation peak at 0.41 V and a reduction peak at 0.33 V in the first cycle of potential. In the second cycle, the oxidation peak shifts about 10 mV toward less positive potentials. The peak-to-peak separation is about 86 mV. These cyclic voltammetric data are consistent with literature reports.[46,54] This process is also well-defined under FTAC voltammetric conditions with a reversible potential of about 0.39 V as determined by analysis of data shown in Figure 6b. Unlike the case of $Co(OH)_2$, well-defined processes associated with further oxidation of NiOOH were not observed in the potential region up to 1 V vs Ag/AgCl under both dc and FTAC voltammetric conditions. On the basis of previous studies,[55−57] process **i** is assigned to the one-electron oxidation of $Ni(OH)_2$ to form NiOOH. The overall reaction giving rise to process **i** is described in eq 5.

DOI: 10.1021/acsami.5b04219
ACS Appl. Mater. Interfaces 2015, 7, 16632−16644

$$Ni(OH)_2 + OH^- \rightleftharpoons NiOOH + H_2O + e^- \quad (5)$$

A current density of 2.1 mA cm^{-2} was achieved for water oxidation with this Ni−Nb film at an overpotential of 480 mV.

3.4. Aging Effects Associated with the Co−Nb and Ni−Nb Films. Previous studies suggest that the catalytic activities of nickel (oxy)hydroxides for water oxidation increase upon aging in alkaline solution due to phase transformation[8,16,54,58] and/or Fe incorporations.[59−61] To confirm this phenomenon and its mechanism, the effect of aging on the catalytic water oxidation activity associated with both Co−Nb and Ni−Nb films was investigated.

Analysis of cyclic voltammograms in Figure 7a shows that in 1 M NaOH solution, the catalytic activity of the Co−Nb film deposited by 20 cycles of potential increases considerably with the aging time. Thus, the catalytic water oxidation current density at 0.8 V increases from 60.2 to 95.8 mA cm^{-2} after 10 min aging, while after 25 min and 1 h aging, the current densities reach 110.2 and 117.2 mA cm^{-2}, respectively. Further aging did not increase the current density. The overpotential required to achieve a current density of 1 mA cm^{-2} decreases from a value of 430 mV by 20 mV and 35 mV with 10 min and 1 h aging, respectively. These results suggest that aging can significantly improve the catalytic activity of the Co−Nb film, especially in the first 10−30 min. However, the peak current for the process at 0.08 V decreases slightly, as does the capacitance upon aging in 1 M NaOH. Analogous changes were also observed for a Co−Nb film deposited with 40 cycles of potential. Figure 7b provides a comparison of FTAC voltammograms before and after aging in 1 M NaOH for 10 and 45 min. The results show that upon aging, the voltammetric characteristics, especially the peak potentials, remain essentially unaltered within experimental uncertainty.

In the case of the Ni−Nb film, the peak potentials for the first redox process detected under dc cyclic voltammetric conditions shift positively upon aging, especially the oxidation process which shifts about 55 mV more positive after aging for 111 min in 1 M NaOH (Figure 8a). This could be due to the phase transformation from α-$Ni(OH)_2$ to β-$Ni(OH)_2$ with the latter undergoing an oxidation reaction to form β-NiOOH at a more positive potential region as suggested in other studies.[16,54,62] The phase transformations and redox processes associated with α-$Ni(OH)_2$ and β-$Ni(OH)_2$ are described in Scheme 1.[60,62] The catalytic activity of the electrode increases significantly with the overpotential required to achieve a current density of 1 mA cm^{-2} decreasing by 53 mV and 80 mV after aging for 10 and 111 min, respectively. The catalytic current detected at 0.75 V vs Ag/AgCl also increases significantly after aging, with a current density increase from 5.4 mA cm^{-2} to 21.6 mA cm^{-2} after 10 min aging, and reaching 52.4 mA cm^{-2} after about 111 min aging and then staying stable with longer aging times. The increase in current and decrease in overpotential suggest improved catalytic water oxidation activity of Ni−Nb film after aging.

Scheme 1. Redox and Phase Transformation of $Ni(OH)_2$ and NiOOH. $E_1^{0\prime}$ and $E_2^{0\prime}$ Are the Reversible Potentials for the Relevant Redox Reactions

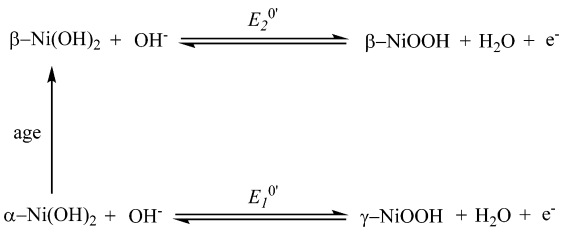

FTAC voltammetric experiments (Figure 8b) were also undertaken to study the effect of aging on the Ni−Nb film. The maximum current associated with the fifth harmonic for the process found at 0.4 V (denoted as i′) in the positive potential scan decreases while a new process at 0.6 V (denoted as i″) emerges upon aging. A similar situation applies to the current detected in the reverse scan of potential which is not included in this figure. Although in dc cyclic voltammograms, only one oxidation process i is observed, with FTAC voltammetry, an additional oxidation process (i″) becomes more obvious after aging. Process i″ increases in current value as process i′ diminishes, and shifts negatively from about 0.6 V by about 40 mV to 0.56 V after 116 min aging. The correlation of the increased current of process i″ and catalytic water oxidation current indicates that process i″ may produce a more active material for water oxidation. In situ Raman[16,46] and spectroelectrochemical studies[63] have suggested a phase transformation occurring in this potential region, with β-NiOOH, generated from β-$Ni(OH)_2$ at higher potential from process i″, being more active than γ-NiOOH. However, dc and FTAC voltammetric data suggest that no catalytic water oxidation is observed in the potential region where β-NiOOH is formed. Therefore, β-NiOOH itself is not directly responsible for the catalytic water oxidation. These experimental observations are consistent with the literature reports which suggest that higher oxidation state of nickel, e.g. Ni^{IV}, is involved in water oxidation.[24−26] Although FTAC voltammetric study provides direct information on the redox chemistry of the active center and the mechanism of Ni-based catalysts, the exact identity of the active form of the catalyst remains unrevealed.

It has been reported that the incorporation of Fe impurities from KOH solution could also be responsible for the observed enhanced catalytic water oxidation activity associated with Ni (oxy)hydroxides aged in unpurified alkaline solution.[59−61] However, our results show that similar patterns of behavior for Co−Nb and Ni−Nb films are observed in both dc cyclic and FTAC voltammetry. Furthermore, the iron and Co/Ni contents in Co−Nb and Ni−Nb films were determined by ICP-OES and ICP-MS before and after aging in 1 M NaOH for 3 h. Iron was not detectable in either film by ICP-OES. Therefore, the observed enhanced catalytic water oxidation activity associated with the aged Ni−Nb films is attributed to the phase transformation resulting in the formation of β-NiOOH. Relatively small enhanced water oxidation activity associated with the aged Co−Nb films, which is not attributable to phase transformation nor the incorporation of Fe impurity, could be due to the physical rearrangement (e.g., through a dissolution/precipitation process) of the film during the aging process.

3.5. Electrodeposition Efficiency of Co−Nb and Ni−Nb Films. To quantify the efficiency of electrodeposition of the Co−Nb film, the cyclic voltammetric experiments summarized in Figure 9a were undertaken. All films were aged in 1 M NaOH for 1 h to maximize the catalytic current. With a large current value of 1×10^{-2} A, even though the R_u of about 10 Ω is low, the ohmic iR_u drop of about 100 mV is substantial. Consequently, iR_u compensation was applied with the measured R_u value in these studies. The film formed in the first cycle produces a current density of 10 mA cm^{-2} for water oxidation at an overpotential of 532 mV. With deposition from

DOI: 10.1021/acsami.5b04219
ACS Appl. Mater. Interfaces 2015, 7, 16632−16644

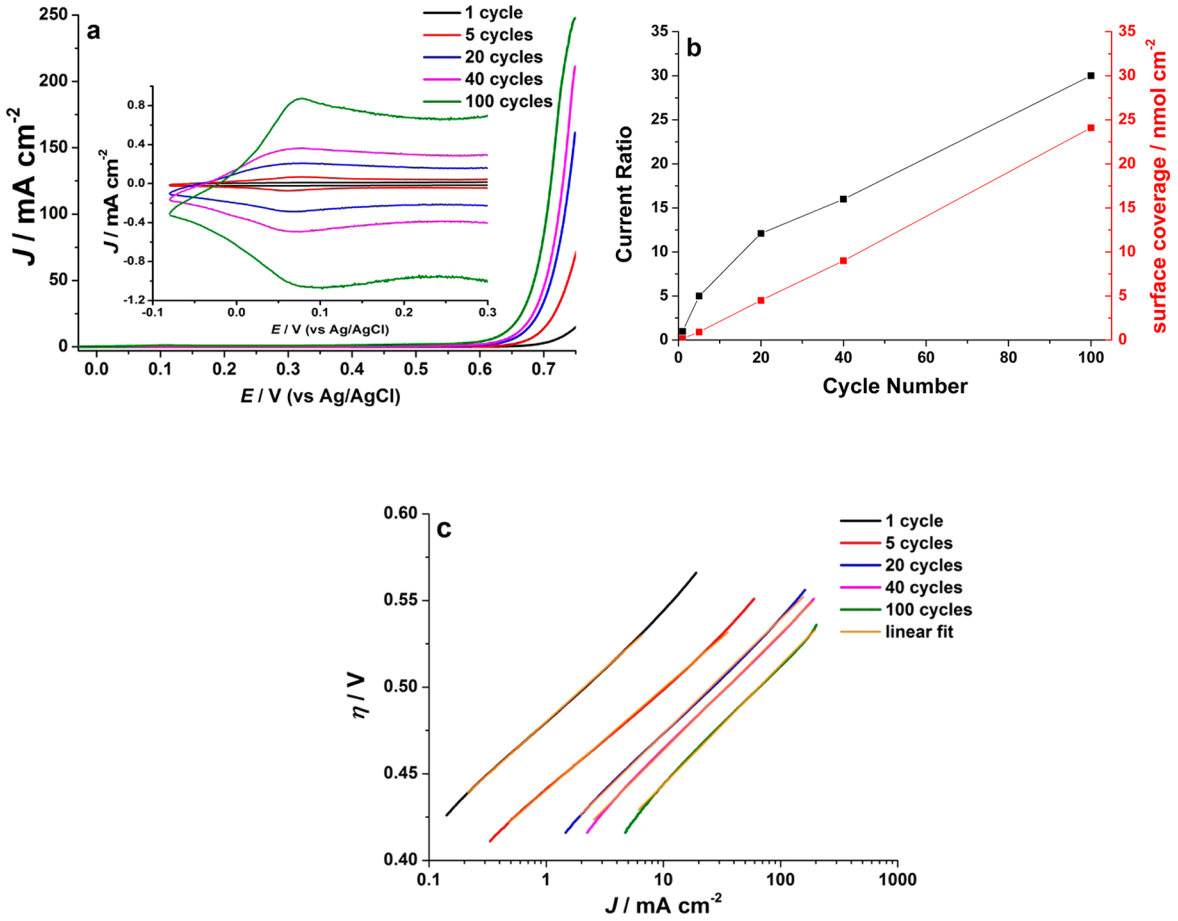

Figure 9. (a) Dc cyclic voltammogram (with iR_u correction) obtained in 1 M NaOH with a scan rate of 0.1 V s^{-1} using a GC electrode (3 mm diameter) modified with a film obtained with 1, 5, 20, 40, and 100 cycles of potential for deposition from a solution containing 5 mM $Co(NO_3)_2$ and 5 mM NbPOM. Inset shows the first cobalt based process in the potential range of −0.1 to +0.3 V. (b) Current ratio (water oxidation current measured at 0.7 V (vs Ag/AgCl) observed for films deposited vs that found at a film deposited for 1 cycle) (black) and surface coverage (red) versus the number of cycles of potential used for modified film deposition. (c) Tafel plots derived from data obtained in (a) with 1, 5, 20, 40, 100 cycles of potential. $\eta = V_{appl} - iR_u - E^{0\prime}$, J = current density.

100 cycles of potential, the overpotential required to produce a 10 mA cm^{-2} current density drops to 438 mV. The surface coverage of cobalt can be calculated from the charge transferred in process **I** (Figure 5a), which involves 2/3 electron per cobalt (eq 2). The charge, after background subtraction, was calculated by integration of the current vs potential data in Figure 5a divided by the scan rate of 0.1 V s^{-1}.[64] The surface coverages of the electroactive Co, calculated from this charge based on Faraday's law (Table 1), increase linearly with the number of cycles of potential (Figure 9b). The catalytic current at 0.7 V vs Ag/AgCl for water oxidation also increases almost linearly with the number of cycles of potential (Figure 9b), which indicates excellent communications between the electrode, the active sites of the catalyst and water. Consequently, the efficiency of this catalyst for the oxidation of water can be enhanced simply by increasing the quantity of catalyst deposited on the electrode surface. Tafel plots derived from analysis of cyclic voltammograms obtained at Co−Nb deposited electrodes are shown in Figure 9c. The constant slopes of 60−70 mV/decade of current density given in Table 1 indicate that the mechanism associated with the Co−Nb film for catalytic water oxidation is not dependent on the number of cycles used for film deposition.

Table 1. Overpotential (η), Surface Coverage, and Slope of Tafel Plots as a Function of Number of Potential Cycles for the Co−Nb Film Formation

no. of deposition cycles	η (mV) at a current density of 10 mA cm^{-2}	surface coverage (nmol cm^{-2})	current ratio[a] at 0.7 V	slope of Tafel plot (mV/decade of current density)
1	532	0.18	1	61
5	487	0.90	5	59
20	461	4.4	12	66
40	452	8.8	16	67
100	438	23.7	30	69

[a]Current ratio = water oxidation current measured at 0.7 V (vs Ag/AgCl) vs that found at a film obtained after a one-cycle of potential for film deposition.

In the case of Ni−Nb film, since phase transformation is significant, cyclic voltammetry (Figure 10a) was undertaken after soaking the modified electrode in 1 M NaOH for 2 h. Under these conditions, the active surface coverage of Ni−Nb film calculated from process **i** which occurs before the onset potential of water oxidation, also increases with the number of cycles of potential for deposition. The deposition efficiency for Ni−Nb film is lower than that for the Co−Nb film judging based on the current magnitude. Therefore, the current ratio

DOI: 10.1021/acsami.5b04219
ACS Appl. Mater. Interfaces 2015, 7, 16632−16644

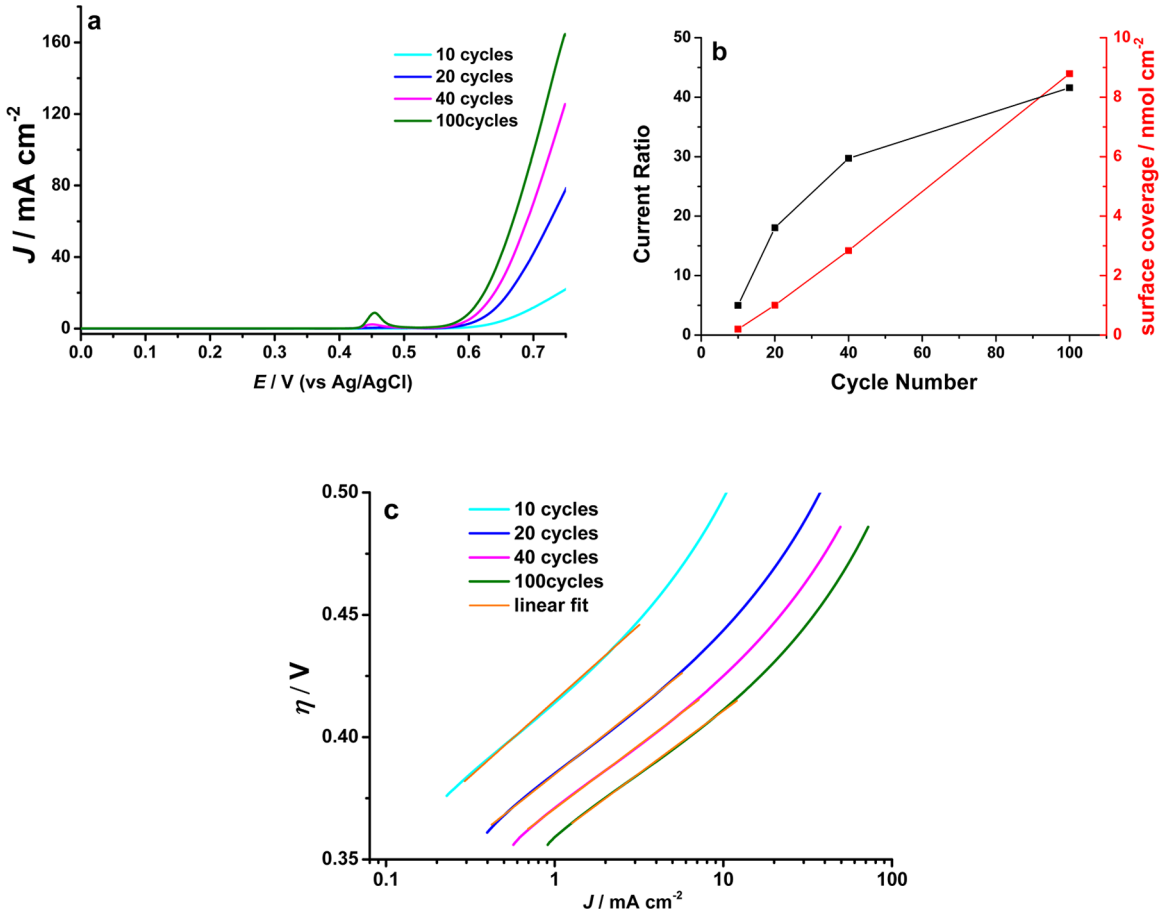

Figure 10. (a) iR_u corrected dc cyclic voltammograms obtained in 1 M NaOH at a scan rate of 0.1 V s^{-1} with a GC electrode (3 mm diameter) modified with a film obtained with 10, 20, 40, and 100 cycles of potential for deposition from a solution containing 5 mM $Ni(NO_3)_2$ and 5 mM NbPOM. The electrode was aged in 1 M NaOH for 2 h before commencing the measurement. (b) Current ratio (water oxidation current measured at 0.7 V (vs Ag/AgCl) observed for films deposited vs that found at a film deposited with 10 cycles of potential) (black) and surface coverage (red) versus the number of cycles of potential used for modified film deposition. (c) Tafel plots derived from data obtained in (a) with 10, 20, 40, and 100 cycles of potential. $\eta = V_{appl} - iR_u - E^{0\prime}$, J = current density.

obtained at 0.7 V vs Ag/AgCl for Ni−Nb film as a function of the number of cycles of potential (Figure 10b) was based on 10 cycles as the reference point instead of 1 cycle of deposition used for the Co modified electrode (Figure 9b). As shown in Figure 10b, the current ratio at 0.7 V increases almost linearly when the number of cycles of potential is less than 40, but then at a slower rate on further cycling of the potential. However, the efficiency of the Co−Nb film modified electrode for water oxidation can still be enhanced by increasing the surface coverage of the catalyst. The calculated surface coverage of the electroactive Ni also increases linearly with the number of cycles of potential (Figure 10b) as for the Co surface coverage in the Co−Nb films. The slopes of the Tafel plots of ∼55 mV/decade for Ni−Nb films are almost independent of the number of potential cycles for film deposition (Figure 10c). This implies that the mechanism associated with the Ni−Nb film for catalytic water oxidation remains unchanged with the number of cycles used for film deposition. The parameters derived from these experiments are summarized in Table 2.

3.6. Stability of the Co−Nb and Ni−Nb Films. The stability and catalytic activity of the Co−Nb and Ni−Nb films also have been examined after aging the electrode in alkaline solution. The stability of the Co−Nb film under catalytic turnover conditions was examined by chronoamperometry using a modified electrode obtained after 20 cycles of potential and aging in 1 M NaOH solution for 1 h. The J−t curve shown in Figure 11a was obtained in 1 M NaOH by applying a constant potential of 0.8 V vs Ag/AgCl for 1000 s. Oxygen formation was so intense that stirring of the solution had to be used to remove the bubbles. The periodic "noise" in the J−t curve is due to bubble detachment from the electrode surface.[65] However, as shown in Figure 11a, the film is stable even under the high current density of about 100 mA cm^{-2} and with hydrodynamic force from stirring and mechanical force associated with bubble formation and removal. A slight decrease in current magnitude was observed with time. This

Table 2. Overpotential (η), Surface Coverage, and Slope of Tafel Plots as a Function of Number of Potential Cycles for Ni−Nb Film Formation

no. of deposition cycles	η (mV) at a current density of 10 mA cm^{-2}	surface coverage (nmol cm^{-2})	current ratio[a] at 0.7 V	slope of Tafel plot (mV/decade of current density)
10	485	0.35	1	62
20	431	1.7	3.6	55
40	412	4.9	5.9	52
100	398	15.2	8.3	51

[a]Current ratio = water oxidation current measured at 0.7 V (vs Ag/AgCl) vs that found at a film obtained after a ten-cycle deposition.

DOI: 10.1021/acsami.5b04219
ACS Appl. Mater. Interfaces 2015, 7, 16632−16644

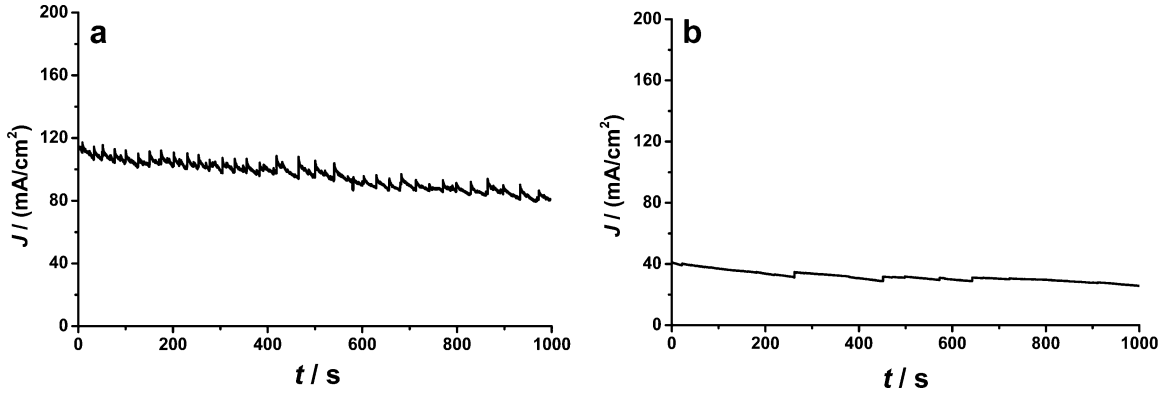

Figure 11. (a) Chronoamperometric data obtained in 1 M NaOH (after aging for 1 h) when the potential was held at 0.8 V for 1000 s with a 3 mm GC electrode modified with a Co−Nb film obtained with 20 cycles of potential for deposition. (b) As for panel a but for the Ni−Nb case, with potential held at 0.75 V with a film obtained after 20 cycles of potential and 2 h of aging.

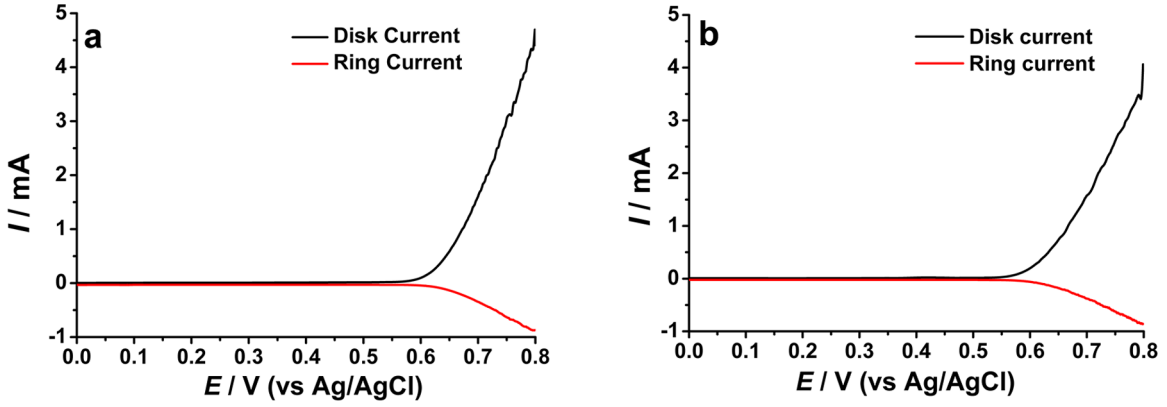

Figure 12. Rotating ring disk electrode voltammograms obtained in 1 M NaOH with a scan rate of 0.02 V s^{-1} and a rotation rate of 104.7 rad s^{-1} with GC disk electrodes modified with an aged (a) Co−Nb and (b) Ni−Nb film obtained with 20 cycles of potential for film deposition. The potential of Pt ring electrode was set at −0.5 V to detect O_2.

is attributed to the blocking of the active sites of the films by O_2 formed because the current completely recovered after the modified electrode was left in solution under open circuit potential for the complete removal of the attached oxygen. SEM images indicate that the morphology of the film is almost unaffected under catalytic water oxidation conditions in 1 M NaOH except for the cracking associated with extensive gas bubbling. Furthermore, the areas associated with the first oxidation process are similar and ICP-MS analysis suggests the Nb and Co contents remain unchanged within experimental uncertainty before and after chronoamperometric experiment, confirming the stability of the film.

Chronoamperometric studies also were performed with a Ni−Nb film aged for 2 h after preparation with 20 cycles of potential. The *J*−*t* data (Figure 11b) obtained with the potential held at 0.75 V shows a similar level of stability but a lower catalytic current density and less "noise" compared to the Co case, which is due to a lower catalyst loading and thus a lower rate of oxygen evolution. Again, the solution was stirred to assist the removal of oxygen bubbles on the electrode surface. The decrease in catalytic current during the chronoamperometric measurement is slightly larger than that found for the Co film, but could be recovered after the modified electrode was left in the solution under open circuit potential for the complete removal of O_2. Furthermore, the areas for the first oxidation process around 0.34 V are similar (i.e., the charges associated with these processes are similar). ICP-MS analysis again suggests that the contents of Ni and Nb remain unchanged within experimental uncertainty before and after the chronoamperometric experiment. Again, SEM images indicate that the morphology of the Ni−Nb film remains essentially unaffected under catalytic water oxidation conditions, as found in the case of Co−Nb film. These data confirm that the Ni−Nb film modified electrode is stable. Although at high overpotential, the iR_u drop is significant, we cannot perform iR_u compensation in these particular experiments due to equipment limitations. Thus, the current densities of Co−Nb and Ni−Nb films are not as high as in Figures 9 and 10, which were obtained after iR_u correction.

3.7. RRDE Detection of Oxygen Generation at Modified Electrodes. In cyclic voltammetric experiments, rapid gas bubble evolution was detected at the modified electrode surface under catalytic turnover conditions, as expected if oxygen is the product of water oxidation. The RRDE method was used with the rate of oxygen formation detected at the Pt ring electrode to quantify the catalytic activity of the film modified disk electrode.[66] In these RRDE measurements, the potential of the rotated disk electrode was scanned from 0 V to +0.8 V using a scan rate of 0.02 V s^{-1} and a rotation rate of 104.7 rad s^{-1}, while a constant potential of −0.5 V was applied to the ring electrode. Oxygen generated at the rotated disk electrode was swept to the Pt ring electrode where it was reduced at the selected potential under mass transport controlled conditions. The process at the disk can be

DOI: 10.1021/acsami.5b04219
ACS Appl. Mater. Interfaces 2015, 7, 16632−16644

described by eq 1, whereas the reaction at the ring electrode corresponds to eq 6[67]

$$\text{reaction at ring electrode: } O_2 + 2H_2O + 2e^- \rightarrow H_2O_2 + 2OH^- \quad (6)$$

The turnover frequency (TOF) and faradaic efficiency for O_2 generation were measured using RRDE. In the case of the films obtained after 20 cycles of potential and 1 h (for the Co−Nb film) or 2 h (for Ni−Nb film) of aging, the ring electrode current for oxygen reduction reached 845 μA with the Co−Nb film (Figure 12a) and 837 μA with the Ni−Nb film (Figure 12b) when the potential at the disk electrode reached its final value of +0.8 V.

The TOF defined as the mole of O_2 production per mole of Co or Ni in the film, is calculated from the oxygen reduction current at the ring electrode, I_R, using the following relationship[68]

$$\text{TOF} = \frac{-I_R}{n_R F A N_{CL} \Gamma} \quad (7)$$

where n_R is the number of electrons transferred per oxygen molecule at the ring electrode (n_R = 2 in 1 M NaOH, eq 6),[67] F is Faraday's constant, A is the area of the disk electrode, Γ is the surface concentration of the catalyst (the population of the Co or Ni sites on the disk electrode), and N_{CL} is the collection efficiency (0.42, as calculated in ref 64).

The faradaic efficiency for O_2 generation, defined as the ratio of the current which is directly due to the formation of O_2 and the total disk current, is calculated from the following relationship[68]

$$\text{Faradaic efficiency} = \left| \frac{I_R n_D}{N_{CL} I_D n_R} \right| \quad (8)$$

where n_D is the number of electrons transferred per oxygen molecule generated at the disk electrode, which is 4 (see eq 1), and I_D and I_R are the disk and ring currents, respectively. At an overpotential of 480 mV, a faradaic efficiency of 92.1% is calculated for Co−Nb film and 96.4% for Ni−Nb film.

Under RRDE conditions, the surface coverage of the electroactive film obtained after 20 cycles of potential is calculated to be 2.0×10^{-9} mol cm^{-2} for the Co−Nb film, and the TOF value is 12.9 s^{-1} at an overpotential of 480 mV, while the values for the Ni−Nb film are 2.3×10^{-9} mol cm^{-2} and 13.2 s^{-1}, respectively. At an overpotential of 590 mV, the TOF values are 41.5 s^{-1} and 35.8 s^{-1} for Co−Nb and Ni−Nb films, respectively. The TOF values are calculated from RRDE data (without iR_u compensation) and use of eq 7. The TOF and Tafel slope values obtained in this study and those for some highly efficient water oxidation catalysts reported in the literature are summarized in Table 3 for comparison. The TOF value of 12.9 s^{-1} for Co−Nb film is higher than that of 1.5 s^{-1} for a CoO_x film[13] and 1.2 s^{-1} (obtained using the known values for TOF and Tafel slope given in Table 3) for a CoOOH film[61] reported by Boettcher and co-workers, but comparable to that of 8.2 s^{-1} for a nickel foam supported Co_3O_4 reported by Esswein et al.[69] at the same overpotential. The TOF value for Co−Nb film at an overpotential of 590 mV is comparable to the value of 34 s^{-1} obtained by Guo et al. under similar conditions with a graphene−cobalt nanocomposite catalyst.[9] The TOF value for Ni−Nb film at an overpotential of 480 mV is comparable to the values of 9.4−15 s^{-1} (obtained using the known values for TOF and Tafel slope given in Table 3) for a $Ni(OH)_2$ film reported by Louie and Bell.[70] However, our TOF value of 13.2 s^{-1} obtained with Ni−Nb films is significantly smaller than the values of 622 and 196 s^{-1} (obtained using the known values for TOF and Tafel slopes given in Table 3), respectively, found at Au and Pd supported α-$Ni(OH)_2$ reported by Yeo et al. at the same overpotential.[16]

Table 3. Comparison of TOF and Tafel Slopes Values at Different Overpotentials in This[a] and Other Studies

catalysts	support electrode	η (mV)	TOF (s^{-1})	Tafel slope (mV/decade)	ref
Co−Nb	GC	480	12.9[b]	73	this work
Co−Nb	GC	590	41.5[b]	73	this work
Co(OOH)	Au	350	0.0052	55	61
Co_3O_4	Ni foam	388	0.09	47	69
CoO_x	Au	480	1.5	42	13
Graphene-Co	GC	590	34[b]	48	9
Ni−Nb	GC	480	13.2[b]	67	this work
Ni−Nb	GC	590	35.8[b]	67	this work
α-$Ni(OH)_2$	Au	350	0.35	~40	16
α-$Ni(OH)_2$	Pd	350	0.11	~40	16
$Ni(OH)_2$	Au	300	0.005−0.008	55	70

[a]Taken from Figure 12. [b]Without iR_u compensation.

4. CONCLUSION

Hexaniobate Lindqvist ions assist the efficient electrodeposition of Co and Ni nanostructures. A mechanism of film formation, involving the electrostatic stabilization of $Co(OH)_2$ or $Ni(OH)_2$ by $[Nb_6O_{19}]^{8-}$, is proposed on the basis of Raman spectroscopic study. SEM images and EDX spectra along with dc cyclic, FTAC and RRDE voltammetry, chronoamperometry and ICP analysis have been used to characterize the morphology, composition, water oxidation catalytic activity and stability in alkaline 1 M NaOH solution. The high TOF values for catalytic oxidation of water obtained from Co and Ni films are comparable to those reported in other studies. An additional Co oxidation process revealed by FTAC voltammetry under catalytic turnover conditions suggests that a Co^{IV} species is likely to be responsible for the high catalytic activities of Co−Nb films. FTAC voltammetric data also suggests that the enhanced catalytic current density associated with the Ni−Nb films after aging in alkaline solution is due to the α to β phase transformation and the electrogenerated higher oxidation state of Ni from β-NiOOH is the more active form of the catalyst.

AUTHOR INFORMATION

Corresponding Authors

*E-mail: jie.zhang@monash.edu. Tel: +61 3 99056289. Fax: +61 3 99054597.

*E-mail: alan.bond@monash.edu. Tel: +61 3 99051338. Fax: +61 3 99054597.

Notes

The authors declare no competing financial interest.

DOI: 10.1021/acsami.5b04219
ACS Appl. Mater. Interfaces 2015, 7, 16632−16644

■ ACKNOWLEDGMENTS

The authors thank the Australian Research Council and Monash University for financial support and the Monash Centre for Electron Microscopy for assistance in obtaining the SEM images and EDX spectra.

■ REFERENCES

(1) Safizadeh, F.; Ghali, E.; Houlachi, G. Electrocatalysis Developments for Hydrogen Evolution Reaction in Alkaline Solutions – A Review. *Int. J. Hydrogen Energy* **2015**, *40*, 256–274.
(2) Nocera, D. G. The Artificial Leaf. *Acc. Chem. Res.* **2012**, *45*, 767–776.
(3) Duan, L.; Bozoglian, F.; Mandal, S.; Stewart, B.; Privalov, T.; Llobet, A.; Sun, L. A Molecular Ruthenium Catalyst with Water-Oxidation Activity Comparable to That of Photosystem II. *Nat. Chem.* **2012**, *4*, 418–423.
(4) Yagi, M.; Kaneko, M. Molecular Catalysts for Water Oxidation. *Chem. Rev.* **2001**, *101*, 21–36.
(5) Fang, Y.-H.; Liu, Z.-P. Mechanism and Tafel Lines of Electro-Oxidation of Water to Oxygen on RuO_2 (110). *J. Am. Chem. Soc.* **2010**, *132*, 18214–18222.
(6) Nakagawa, T.; Bjorge, N. S.; Murray, R. W. Electrogenerated IrO_x Nanoparticles as Dissolved Redox Catalysts for Water Oxidation. *J. Am. Chem. Soc.* **2009**, *131*, 15578–15579.
(7) Lyons, M. E.; Brandon, M. P. The Oxygen Evolution Reaction on Passive Oxide Covered Transition Metal Electrodes in Alkaline Solution Part II-Cobalt. *Int. J. Electrochem. Sci.* **2008**, *3*, 1425–1462.
(8) Lyons, M. E.; Brandon, M. P. The Oxygen Evolution Reaction on Passive Oxide Covered Transition Metal Electrodes in Aqueous Alkaline Solution. Part 1—Nickel. *Int. J. Electrochem. Sci.* **2008**, *3*, 1386–1424.
(9) Guo, S.-X.; Liu, Y.; Bond, A. M.; Zhang, J.; Esakki Karthik, P.; Maheshwaran, I.; Senthil Kumar, S.; Phani, K. L. N. Facile Electrochemical Co-Deposition of a Graphene-Cobalt Nanocomposite for Highly Efficient Water Oxidation in Alkaline Media: Direct Detection of Underlying Electron Transfer Reactions under Catalytic Turnover Conditions. *Phys. Chem. Chem. Phys.* **2014**, *16*, 19035–19045.
(10) Singh, A.; Chang, S. L.; Hocking, R. K.; Bach, U.; Spiccia, L. Highly Active Nickel Oxide Water Oxidation Catalysts Deposited from Molecular Complexes. *Energy Environ. Sci.* **2013**, *6*, 579–586.
(11) Rosen, J.; Hutchings, G. S.; Jiao, F. Ordered Mesoporous Cobalt Oxide as Highly Efficient Oxygen Evolution Catalyst. *J. Am. Chem. Soc.* **2013**, *135*, 4516–4521.
(12) Gao, M.; Sheng, W.; Zhuang, Z.; Fang, Q.; Gu, S.; Jiang, J.; Yan, Y. Efficient Water Oxidation Using Nanostructured α-Nickel-Hydroxide as an Electrocatalyst. *J. Am. Chem. Soc.* **2014**, *136*, 7077–7084.
(13) Trotochaud, L.; Ranney, J. K.; Williams, K. N.; Boettcher, S. W. Solution-Cast Metal Oxide Thin Film Electrocatalysts for Oxygen Evolution. *J. Am. Chem. Soc.* **2012**, *134*, 17253–17261.
(14) Palmas, S.; Ferrara, F.; Pisu, A.; Cannas, C. Oxygen Evolution on Ti/Co_3O_4-Coated Electrodes in Alkaline Solution. *Chem. Pap.* **2007**, *61*, 77–82.
(15) Casella, I. G.; Gatta, M. Study of the Electrochemical Deposition and Properties of Cobalt Oxide Species in Citrate Alkaline Solutions. *J. Electroanal. Chem.* **2002**, *534*, 31–38.
(16) Yeo, B. S.; Bell, A. T. In Situ Raman Study of Nickel Oxide and Gold-Supported Nickel Oxide Catalysts for the Electrochemical Evolution of Oxygen. *J. Phys. Chem. C* **2012**, *116*, 8394–8400.
(17) Watanabe, T. *Nano Plating—Microstructure Formation Theory of Plated Films and a Database of Plated Films*; Elsevier: Oxford, U.K., 2004.
(18) Kanan, M. W.; Nocera, D. G. In Situ Formation of an Oxygen-Evolving Catalyst in Neutral Water Containing Phosphate and Co^{2+}. *Science* **2008**, *321*, 1072–1075.
(19) Surendranath, Y.; Dinca, M.; Nocera, D. G. Electrolyte-Dependent Electrosynthesis and Activity of Cobalt-Based Water Oxidation Catalysts. *J. Am. Chem. Soc.* **2009**, *131*, 2615–2620.
(20) Lutterman, D. A.; Surendranath, Y.; Nocera, D. G. A Self-Healing Oxygen-Evolving Catalyst. *J. Am. Chem. Soc.* **2009**, *131*, 3838–3839.
(21) Surendranath, Y.; Lutterman, D. A.; Liu, Y.; Nocera, D. G. Nucleation, Growth, and Repair of a Cobalt-Based Oxygen Evolving Catalyst. *J. Am. Chem. Soc.* **2012**, *134*, 6326–6336.
(22) Gerken, J. B.; McAlpin, J. G.; Chen, J. Y. C.; Rigsby, M. L.; Casey, W. H.; Britt, R. D.; Stahl, S. S. Electrochemical Water Oxidation with Cobalt-Based Electrocatalysts from pH 0–14: The Thermodynamic Basis for Catalyst Structure, Stability, and Activity. *J. Am. Chem. Soc.* **2011**, *133*, 14431–14442.
(23) Lu, P.; Srinivasan, S. Electrochemical-Ellipsometric Studies of Oxide Film Formed on Nickel During Oxygen Evolution. *J. Electrochem. Soc.* **1978**, *125*, 1416–1422.
(24) Corrigan, D. A.; Knight, S. L. Electrochemical and Spectroscopic Evidence on the Participation of Quadrivalent Nickel in the Nickel Hydroxide Redox Reaction. *J. Electrochem. Soc.* **1989**, *136*, 613–619.
(25) Juodkazis, K.; Juodkazytė, J.; Vilkauskaitė, R.; Jasulaitienė, V. Nickel Surface Anodic Oxidation and Electrocatalysis of Oxygen Evolution. *J. Solid State Electrochem.* **2008**, *12*, 1469–1479.
(26) Bediako, D. K.; Lassalle-Kaiser, B.; Surendranath, Y.; Yano, J.; Yachandra, V. K.; Nocera, D. G. Structure–Activity Correlations in a Nickel–Borate Oxygen Evolution Catalyst. *J. Am. Chem. Soc.* **2012**, *134*, 6801–6809.
(27) Pope, M. T. *Heteropoly and Isopoly Oxometalates*; Springer–Verlag: Weinheim, Germany, 1983; Vol. *8*.
(28) Hill, C. L. Introduction: Polyoxometalatesmulticomponent Molecular Vehicles to Probe Fundamental Issues and Practical Problems. *Chem. Rev.* **1998**, *98*, 1–2.
(29) Sadakane, M.; Steckhan, E. Electrochemical Properties of Polyoxometalates as Electrocatalysts. *Chem. Rev.* **1998**, *98*, 219–237.
(30) Troupis, A.; Hiskia, A.; Papaconstantinou, E. Synthesis of Metal Nanoparticles by Using Polyoxometalates as Photocatalysts and Stabilizers. *Angew. Chem., Int. Ed.* **2002**, *41*, 1911–1914.
(31) Zhang, J.; Ting, B. P.; Koh, Y. T.; Ying, J. Y. Synthesis of Metallic Nanoparticles Using Electrogenerated Reduced Forms of $[\alpha\text{-}SiW_{12}O_{40}]^{4-}$as Both Reductants and Stabilizing Agents. *Chem. Mater.* **2011**, *23*, 4688–4693.
(32) Black, J. R.; Nyman, M.; Casey, W. H. Rates of Oxygen Exchange between the $[H_xNb_6O_{19}]^{8-x}$ (aq) Lindqvist Ion and Aqueous Solutions. *J. Am. Chem. Soc.* **2006**, *128*, 14712–14720.
(33) Villa, E. M.; Ohlin, C. A.; Casey, W. H. Oxygen-Isotope Exchange Rates for Three Isostructural Polyoxometalate Ions. *J. Am. Chem. Soc.* **2010**, *132*, 5264–5272.
(34) Etxebarria, N.; Fernandez, L. A.; Madariaga, J. M. On the Hydrolysis of Niobium(V) and Tantalum(V) in 3 mol dm^{-3} KCl at 25 ^{o}C. Part 1. Construction of a Thermodynamic Model for Nb^{v}. *J. Chem. Soc., Dalton Trans.* **1994**, 3055–3059.
(35) Britton, H. T. S.; Robinson, R. A. 322. Physicochemical Studies of Complex Acids. Part VIII. Niobic Acid. *J. Chem. Soc.* **1932**, 2265–2270.
(36) Niu, J.; Li, F.; Zhao, J.; Ma, P.; Zhang, D.; Bassil, B.; Kortz, U.; Wang, J. Tetradecacobalt (II)-Containing 36-Niobate $[Co_{14}(OH)_{16}(H_2O)_8Nb_{36}O_{106}]^{20-}$ and Its Photocatalytic H_2 Evolution Activity. *Chem. - Eur. J.* **2014**, *20*, 9852–9857.
(37) Chen, G.; Ma, P.; Wang, J.; Niu, J. A New Organic–Inorganic Hybrid Polyoxoniobate Based on Lindqvist-Type Anion and Nickel Complex. *J. Coord. Chem.* **2010**, *63*, 3753–3763.
(38) Flynn, C. M., Jr; Stucky, G. D. Sodium 6-Niobo (Ethylenediamine) Cobaltate (III) and Its Chromate (III) Analog. *Inorg. Chem.* **1969**, *8*, 178–180.
(39) Flynn, C. M., Jr; Stucky, G. D. Heteropolyniobate Complexes of Manganese (IV) and Nickel (IV). *Inorg. Chem.* **1969**, *8*, 332–334.
(40) Bond, A. M.; Duffy, N. W.; Guo, S.-X.; Zhang, J.; Elton, D. Changing the Look of Voltammetry. *Anal. Chem.* **2005**, *77*, 186 A–195 A.

DOI: 10.1021/acsami.5b04219
ACS Appl. Mater. Interfaces 2015, 7, 16632–16644

(41) Guo, S.-X.; Bond, A. M.; Zhang, J. Fourier Transformed Large Amplitude Alternating Current Voltammetry: Principles and Applications. *Rev. Polarogr.* **2015**, *61*, 21−32.
(42) Sawyer, D. T.; Sobkowiak, A.; Roberts, J. L. *Electrochemistry for Chemists*, 2nd ed.; Wiley-Interscience: New York, 1995.
(43) Antonio, M. R.; Nyman, M.; Anderson, T. M. Direct Observation of Contact Ion-Pair Formation in Aqueous Solution. *Angew. Chem., Int. Ed.* **2009**, *48*, 6136−6140.
(44) Shieh, S. R.; Duffy, T. S. Raman Spectroscopy of $Co(OH)_2$ at High Pressures: Implications for Amorphization and Hydrogen Repulsion. *Phys. Rev. B: Condens. Matter Mater. Phys.* **2002**, *66*, 134301.
(45) Koza, J. A.; Hull, C. M.; Liu, Y.-C.; Switzer, J. A. Deposition of β-$Co(OH)_2$ Films by Electrochemical Reduction of Tris-(Ethylenediamine)Cobalt(III) in Alkaline Solution. *Chem. Mater.* **2013**, *25*, 1922−1926.
(46) Lo, Y. L.; Hwang, B. J. In Situ Raman Studies on Cathodically Deposited Nickel Hydroxide Films and Electroless Ni−P Electrodes in 1 M KOH Solution. *Langmuir* **1998**, *14*, 944−950.
(47) Zhang, J.; Bond, A. M. Theoretical Studies of Large Amplitude Alternating Current Voltammetry for a Reversible Surface-Confined Electron Transfer Process Coupled to a Pseudo First-Order Electrocatalytic Process. *J. Electroanal. Chem.* **2007**, *600*, 23−34.
(48) Guo, S.-X.; Zhang, J.; Elton, D. M.; Bond, A. M. Fourier Transform Large-Amplitude Alternating Current Cyclic Voltammetry of Surface-Bound Azurin. *Anal. Chem.* **2003**, *76*, 166−177.
(49) Zhang, J.; Guo, S.-X.; Bond, A. M. Discrimination and Evaluation of the Effects of Uncompensated Resistance and Slow Electrode Kinetics from the Higher Harmonic Components of a Fourier Transformed Large-Amplitude Alternating Current Voltammogram. *Anal. Chem.* **2007**, *79*, 2276−2288.
(50) Pourbaix, M. *Atlas of Electrochemical Equilibria in Aqueous Solutions*; National Association of Corrosion Engineers: Houston, TX, 1974.
(51) Pontinha, M.; Faty, S.; Walls, M. G.; Ferreira, M. G. S.; Da Cunha Belo, M. Electronic Structure of Anodic Oxide Films Formed on Cobalt by Cyclic Voltammetry. *Corros. Sci.* **2006**, *48*, 2971−2986.
(52) Kanan, M. W.; Yano, J.; Surendranath, Y.; Dincă, M.; Yachandra, V. K.; Nocera, D. G. Structure and Valency of a Cobalt−Phosphate Water Oxidation Catalyst Determined by in Situ X-Ray Spectroscopy. *J. Am. Chem. Soc.* **2010**, *132*, 13692−13701.
(53) Liu, Y.; Guo, S.-X.; Bond, A. M.; Zhang, J.; Geletii, Y. V.; Hill, C. L. Voltammetric Determination of the Reversible Potentials for $[\{Ru_4O_4(OH)_2(H_2O)_4\}(\gamma\text{-}SiW_{10}O_{36})_2]^{10-}$ over the pH Range of 2−12: Electrolyte Dependence and Implications for Water Oxidation Catalysis. *Inorg. Chem.* **2013**, *52*, 11986−11996.
(54) Godwin, I. J.; Lyons, M. E. G. Enhanced Oxygen Evolution at Hydrous Nickel Oxide Electrodes Via Electrochemical Ageing in Alkaline Solution. *Electrochem. Commun.* **2013**, *32*, 39−42.
(55) Kostecki, R.; McLarnon, F. Electrochemical and in Situ Raman Spectroscopic Characterization of Nickel Hydroxide Electrodes: I. Pure Nickel Hydroxide. *J. Electrochem. Soc.* **1997**, *144*, 485−493.
(56) Cappadonia, M.; Divisek, J.; von der Heyden, T.; Stimming, U. Oxygen Evolution at Nickel Anodes in Concentrated Alkaline Solution. *Electrochim. Acta* **1994**, *39*, 1559−1564.
(57) Lu, P. W. T.; Srinivasan, S. Electrochemical-Ellipsometric Studies of Oxide Film Formed on Nickel During Oxygen Evolution. *J. Electrochem. Soc.* **1978**, *125*, 1416−1422.
(58) Oliva, P.; Leonardi, J.; Laurent, J.; Delmas, C.; Braconnier, J.; Figlarz, M.; Fievet, F.; De Guibert, A. Review of the Structure and the Electrochemistry of Nickel Hydroxides and Oxy-Hydroxides. *J. Power Sources* **1982**, *8*, 229−255.
(59) Trotochaud, L.; Young, S. L.; Ranney, J. K.; Boettcher, S. W. Nickel−Iron Oxyhydroxide Oxygen-Evolution Electrocatalysts: The Role of Intentional and Incidental Iron Incorporation. *J. Am. Chem. Soc.* **2014**, *136*, 6744.
(60) Klaus, S.; Cai, Y.; Louie, M. W.; Trotochaud, L.; Bell, A. T. Effects of Fe Electrolyte Impurities on $Ni(OH)_2$/NiOOH Structure and Oxygen Evolution Activity. *J. Phys. Chem. C* **2015**, *119*, 7243−7254.
(61) Burke, M. S.; Kast, M. G.; Trotochaud, L.; Smith, A. M.; Boettcher, S. W. Cobalt−Iron (Oxy) Hydroxide Oxygen Evolution Electrocatalysts: The Role of Structure and Composition on Activity, Stability, and Mechanism. *J. Am. Chem. Soc.* **2015**, *137*, 3638−3648.
(62) Barnard, R.; Randell, C. F.; Tye, F. L. Studies Concerning Charged Nickel Hydroxide Electrodes I. Measurement of Reversible Potentials. *J. Appl. Electrochem.* **1980**, *10*, 109−125.
(63) Zhang, C.; Park, S. M. In Situ Spectroelectrochemical Studies on the Anodic Oxidation of Nickel Hydroxide in Alkaline Media. *J. Electrochem. Soc.* **1989**, *136*, 3333−3342.
(64) Guo, S.-X.; Liu, Y.; Lee, C.-Y.; Bond, A. M.; Zhang, J.; Geletii, Y. V.; Hill, C. L. Graphene-Supported $[\{Ru_4O_4(OH)_2(H_2O)_4\}(\gamma\text{-}SiW_{10}O_{36})_2]^{10-}$ for Highly Efficient Electrocatalytic Water Oxidation. *Energy Environ. Sci.* **2013**, *6*, 2654−2663.
(65) Minguzzi, A.; Fan, F.-R. F.; Vertova, A.; Rondinini, S.; Bard, A. J. Dynamic Potential-pH Diagrams Application to Electrocatalysts for Water Oxidation. *Chem. Sci.* **2012**, *3*, 217−229.
(66) Bard, A. J.; Faulkner, L. R. *Electrochemical Methods: Fundamentals and Applications*, 2nd ed.; Wiley: New York, 2001; Vol. 2.
(67) Zhang, C.; Fan, F.-R. F.; Bard, A. J. Electrochemistry of Oxygen in Concentrated NaOH Solutions: Solubility, Diffusion Coefficients, and Superoxide Formation. *J. Am. Chem. Soc.* **2008**, *131*, 177−181.
(68) Liu, Y.; Guo, S.-X.; Bond, A. M.; Zhang, J.; Du, S. Cobalt (II) Phosphonate Coordination Polymers: Synthesis, Characterization and Application as Oxygen Evolution Electrocatalysts in Aqueous Media and Water-Saturated Hydrophobic 1-Butyl-3-Methylimidazolium Hexafluorophosphate Ionic Liquid. *Electrochim. Acta* **2013**, *101*, 201−208.
(69) Esswein, A. J.; McMurdo, M. J.; Ross, P. N.; Bell, A. T.; Tilley, T. D. Size-Dependent Activity of Co_3O_4 Nanoparticle Anodes for Alkaline Water Electrolysis. *J. Phys. Chem. C* **2009**, *113*, 15068−15072.
(70) Louie, M. W.; Bell, A. T. An Investigation of Thin-Film Ni−Fe Oxide Catalysts for the Electrochemical Evolution of Oxygen. *J. Am. Chem. Soc.* **2013**, *135*, 12329−12337.

DOI: 10.1021/acsami.5b04219
ACS Appl. Mater. Interfaces 2015, 7, 16632−16644